J. Plasma Physics (2006), *vol.* 72, *part* 4, *pp.* 491–506. © 2006 Cambridge University Press
doi:10.1017/S0022377805004241 First published online 11 January 2006 Printed in the United Kingdom

Magnetohydrodynamic simulation of two capillary discharge channels

CHUN MEI WANG, R. KEPPENS and J. P. GOEDBLOED

FOM-Institute for Plasma Physics 'Rijnhuizen', PO Box 1207, 3430 BE, Nieuwegein, The Netherlands
(www.rijnh.nl)

(Received 2005 and in revised form 2005)

Abstract. Two plasma channels, corresponding to a slow capillary discharge and a fast capillary discharge plasma, are investigated numerically. A long-lifetime parabolic plasma channel is formed in the slow capillary discharge channel. Its radial density profile is determined by the energy balance between Ohmic heating and thermal conduction, together with force balance. The profile and the on-axis density value vary only weakly with the peak value of the slow discharge current (300–600 A). A rather dynamic plasma channel is formed under the compression by a magnetic piston in the fast capillary discharge channel. In a narrow time window of the order of nanoseconds a suitable hollow relatively low density channel is reached, followed by a shock-dominated rebound phase. The on-axis density minimum features of these two channels make both of them suitable guiding channels for the laser wakefield accelerators. In particular, a low-density channel ($n_e \sim 5 \times 10^{16}$ cm^{-3}) formed in the fast capillary discharge is in favor of controlled beam injection, but requires precise timing, while the slow capillary discharge is in essence steady. We discuss possible strategies for using them in a segmented approach.

1. Introduction

In the standard laser wakefield accelerator (LWFA) [1], a laser pulse traveling in a plasma induces a force known as the ponderomotive force, $F_{\rm pond}$, which is proportional to the gradient of the laser intensity $F_{\rm pond} \propto \nabla I_{\rm laser}$. The ponderomotive force excites plasma electron oscillations. This plasma wave propagates with a phase velocity $v_{\rm ph}$ close to the speed of light c, and can trap and accelerate electrons. Owing to the large number of free electrons oscillating in the plasma, high acceleration gradients are reachable, e.g. accelerating gradients of 1 GV cm^{-1} are possible for a plasma density of 10^{18} cm^{-3}. Such an accelerating gradient is more than a thousand times larger than in conventional accelerators. This aspect of plasma accelerators is what makes them promising candidates for compact next-generation accelerators.

A high-intensity laser pulse is necessary to develop a high-energy accelerator. For instance, to create a plasma wave suitable for acceleration, the light intensity must be high, $I > 10^{17}$ W cm^{-1}. Below this value, a plasma wave with small amplitude cannot effectively accelerate particles. In the absence of optical guiding, the intense laser pulse spreads quickly, owing to the natural tendency for a tightly focused pulse

https://doi.org/10.1017/S0022377805004241 Published online by Cambridge University Press

to spread. The corresponding characteristic distance is the Rayleigh length $Z_R = \pi r_0^2/\lambda_0$, where r_0 is the laser spot radius at the focus and λ_0 is the laser wavelength. For instance, the intensity of a light beam with $r_0 = 30$ μm and $\lambda_0 = 1$ μm will drop significantly over 3 μm. Extending the acceleration length beyond Z_R requires optical guiding. This can be achieved with a preformed plasma channel [2–4].

In addition to Rayleigh diffraction, dephasing of electrons in the wakefield also limits the energy gain [5–7]. This limit occurs since the accelerated electrons ($v_e \approx c$), which are initially in phase with the accelerating field, will in time outrun the accelerating field ($v_{ph} < c$) and enter a decelerating region. Recently, three groups [8–10] simultaneously found a new physical region where self-injected electrons can reach approximately the same energy with a high acceleration rate (∼100 MeV). The formation of such monoenergetic electron beams is only possible when the acceleration distance matches the dephasing length. To achieve a monoenergetic electron beam, the interaction length between the accelerated particles and the accelerating wakefield needs to be equal to or shorter than the dephasing length. Hence, instead of the interaction length, it is the dephasing length that essentially limits the acceleration distance.

A tapered channel, where the plasma density increases along the laser propagation path, has been proposed to mitigate the dephasing problem. In a finely tapered plasma channel, the phase velocity of the wakefield can equal the speed of light [11, 12]. For example, a luminous point is found behind the pulse if the plasma density increases from 10^{17} to 10^{18} cm^{-3} over a distance of 50 Z_R for a given laser pulse. To create a tapered channel, a capillary made out of several segments was introduced [13], where each segment is connected to a separate capacitor. A change in the voltage of each capacitor provides a change in the current through each segment, which is meant to 'taper' the plasma density in a multi-stage approach. A density variation from 1.0×10^{19} to 2.3×10^{19} cm^{-3} within 6 cm was reported in this segmented discharge.

For given laser parameters, there is a trade-off in choosing the optimal electron number density n_e. From the dephasing length $L_d \propto \lambda_0^{-2} n_e^{-3/2}$ [14], a low density n_e is required to minimize the phase slippage, whereas a high density is necessary to maximize the peak accelerating field E_z^{peak} due to the fact that it scales as $n_e^{1/2}$ [15]. The maximum electron energy $W = eL_d E^{peak}$ is proportional to n_e^{-1}. Therefore, provided the driving laser pulse can be guided over the dephasing length, the electron energy produced by laser wakefield acceleration increases as the electron density is reduced. Operating in a low-density plasma has another advantage: the plasma wavelength is longer. The long wavelength makes it easier to inject a bunch of electrons into the plasma wave, since the bunch length must be short compared to the plasma wavelength λ_p.

In this paper, we explore numerically two different capillary discharge plasma channels, namely a slow capillary discharge and a fast capillary discharge.

(i) In the slow capillary discharge channel, a low (300 A) and slow rising (risetime $t = 100$ ns) discharge current is used. Once fully ionized, the plasma in this capillary is shown to reach a thermodynamic equilibrium where the resistive diffusion time is much faster than sonic or Alfvén transit times. Together with effective thermal conduction, this results in radial variations of the density, the pressure and the current density of a fairly global character. Whereas plasma cooling at the wall leads to a density minimum on-axis.

https://doi.org/10.1017/S0022377805004241 Published online by Cambridge University Press

(ii) In the fast discharge capillary, a high (5 kA) and fast rising (risetime $t = 15$ ns) discharge current is used. Since Ohmic heating increases the temperature, and thus the Spitzer conductivity early in the current rise, the thermal conductivity fairly quickly becomes large enough that the magnetic field cannot penetrate, so that a current sheet is formed along the wall. This current sheet moves along with the plasma inwards. The plasma accumulates and the density peaks at the current sheet. Shortly before the plasma collapses on the axis, a concave guiding channel is formed.

This paper is organized as follows. In Sec. 2, we present the one-fluid magnetohydrodynamic (MHD) model of the capillary discharge. In Sec. 3, we discuss the time scales of the two capillary discharges. Numerical studies on the plasma dynamics of the slow and fast discharges are presented in Sec. 4. Finally, a discussion of possible segmented approach using these discharges and conclusions are given in Sec. 5.

2. MHD model

To study the dynamics of the capillary discharge plasma channels, the one-fluid MHD equations are adopted. The use of one-fluid MHD modeling in this section is validated by independent, more sophisticated studies of the capillary discharge evolution by Hosokai et al. [2], Bobrova et al. [16] and Broks et al. [17]. The stage of almost full ionization is reached within 50 ns for the slow discharge. As shown by Broks et al., strong non-local thermal equilibrium (non-LTE) effects occur in the first 50 ns. After that, the plasma tends to be in thermal equilibrium, and the difference between the electron temperature T_e and the ion temperature T_i is negligible. Hence, we take these results as a starting point and can then assume that our plasma has been ionized already, so that from that point onwards (corresponding to 50 ns for the slow discharge stage and 4.5 ns for the fast discharge stage based on the numerical study of Hosokai et al.) our investigation can ignore ionization or radiation processes. For simplicity, we describe the plasma in one-dimensional cylindrical symmetry, so that the dependent variables are functions of radius r and time t only. The magnetic field is restricted to the azimuthal direction, since the current flows along the channel axis (in the z direction), whereas only a radial plasma velocity occurs. Hence, the plasma is described by four variables, namely the density ρ, the radial momentum density ρv_r, the azimuthal field component B_θ and the internal energy density ρe.

The MHD equations are written in conservative form, so that a conservative numerical difference scheme may be employed. They express conservation of mass,

$$\frac{\partial \rho}{\partial t} + \nabla \cdot (\rho \mathbf{v}) = 0, \tag{2.1}$$

conservation of momentum,

$$\frac{\partial}{\partial t}(\rho \mathbf{v}) + \nabla \cdot \left[\rho \mathbf{v}\mathbf{v} + \left(p + \frac{1}{2\mu_0} B^2\right)\mathbf{I} - \frac{\mathbf{B}\mathbf{B}}{\mu_0}\right] = 0, \tag{2.2}$$

and (near) conservation of magnetic flux,

$$\frac{\partial \mathbf{B}}{\partial t} + \nabla \cdot (\mathbf{v}\mathbf{B} - \mathbf{B}\mathbf{v}) = -\frac{1}{\mu_0} \nabla \times (\eta \nabla \times \mathbf{B}). \tag{2.3}$$

https://doi.org/10.1017/S0022377805004241 Published online by Cambridge University Press

Here, ρ, $\mathbf{v}$, p and $\mathbf{B}$ denote the plasma density, the velocity, the pressure and the magnetic field, respectively. $\mathbf{I}$ is the identity matrix and μ_0 is the permeability of vacuum. The resistivity η is generally temperature dependent. In our simulation we employ the Spitzer formula $\eta = \eta_0 T^{-3/2}$ (Ωm), where $\eta_0 \approx 65 Z \ln\Lambda$ (ΩmK$^{3/2}$), $[T] = $ K [18], Z is the charge number of the ions and $\ln\Lambda$ is the Coulomb logarithm.

While an equation in conservation form may be written for the total energy density, we exploit an equation governing the thermal energy density in which the internal energy losses by thermal conduction and energy gains by Ohmic heating appear explicitly:

$$\frac{d}{dt}(\rho e) + \gamma \rho e \nabla \cdot \mathbf{v} = \eta j^2 + \nabla \cdot (\boldsymbol{\kappa} \cdot \nabla T). \tag{2.4}$$

Here, e is the internal energy per unit mass defined by

$$e \equiv \frac{1}{\gamma - 1}\frac{p}{\rho} \equiv \mathscr{R}\frac{T}{\gamma - 1}, \tag{2.5}$$

see (7.17) of [19], where $\mathscr{R} \equiv k/(\tilde{\mu} m_{\mathrm{p}})$ is the gas constant, $\tilde{\mu}$ is the mean molecular weight, k and m_{p} are the Boltzmann constant and the proton mass, respectively. The current density $\mathbf{j}$ is defined by Ampere's law,

$$\mathbf{j} = \frac{1}{\mu_0}\nabla \times \mathbf{B}. \tag{2.6}$$

The convective time derivative $d/dt \equiv \partial/\partial t + \mathbf{v} \cdot \nabla$. The ratio of specific heats, γ, is assumed to be $\frac{5}{3}$. We have ignored the role of radiation in (2.4). If one deals with heavier elements in fast discharges, the energy losses through radiation may become important.

The right-hand side of (2.4) contains two terms, namely the energy gained through Ohmic heating, and the energy losses (or gains) through thermal conduction. In the thermal conduction term, $\boldsymbol{\kappa}$ is the anisotropic thermal conductivity tensor. In a strong magnetic field, thermal conduction across the magnetic field is inhibited, whereas conduction along the field is unaffected. Thus, to a good approximation, thermal conduction is given by

$$\nabla \cdot (\boldsymbol{\kappa} \cdot \nabla T) \approx \nabla \cdot \left(\kappa_{\parallel} \frac{\mathbf{BB}}{B^2} \cdot \nabla T\right) + \nabla \cdot (\kappa_{\perp} \nabla T), \tag{2.7}$$

with $\kappa_{\parallel} = \kappa_0 T^{5/2}$ (W K^{-1} m^{-1}), where $\kappa_0 \approx 2.4 \times 10^{-10} (Z \ln\Lambda)^{-1}$ (W K$^{-7/2}$ m^{-1}), $[T] = K$ [19]. Since we describe the plasma in one-dimensional cylindrical symmetry, and the magnetic field is restricted to the azimuthal direction, the first term on the right-hand side of (2.7) drops out for both slow and fast discharge capillaries. In the weakly magnetized slow discharge stage, the thermal conductivity is isotropic, $\kappa_{\perp} = \kappa_{\parallel}$. In the strongly magnetized fast discharge stage, $\kappa_{\perp} \approx 0$, as evaluated in Sec. 3, so that transport across the magnetic field is forbidden.

For the numerical simulation, we transform the MHD equations to dimensionless form by a proper choice for the units of length, mass and time. Length is normalized by the capillary radius R, the density is normalized by the density ρ_0 on-axis, and time is normalized by the transit time of a sound wave over the capillary radius, $\tau_{\mathrm{s}0} \equiv R/v_{\mathrm{s}0}$ (the sound speed on-axis $v_{\mathrm{s}0} = \sqrt{\gamma p_0/\rho_0}$). All the variables are made dimensionless by means of R, ρ_0 and $v_{\mathrm{s}0}$, so that

$$\bar{\mathbf{r}} \equiv \mathbf{r}/R, \quad \bar{T} \equiv T/(v_{\mathrm{s}0}^2 \mathscr{R}^{-1}),$$

$$\bar{t} = t/\tau_{\mathrm{s}0}, \quad \bar{\mathbf{B}} \equiv \mathbf{B}/\sqrt{\mu_0 \rho_0 v_{\mathrm{s}0}^2},$$

https://doi.org/10.1017/S0022377805004241 Published online by Cambridge University Press

$$\bar{\rho} \equiv \rho/\rho_0, \quad \bar{\mathbf{j}} \equiv \mathbf{j}/(v_{s0}\sqrt{\rho}(R\sqrt{\mu_0})^{-1}),$$
$$\bar{\mathbf{v}} \equiv \mathbf{v}/v_{s0}, \quad \bar{\eta}_0 \equiv \eta_0/(\mu_0 v_{s0}^4 R\mathscr{R}^{-3/2}),$$
$$\bar{e} \equiv e/v_{s0}^2, \quad \bar{\kappa}_0 \equiv \kappa_0/(\rho_0 v_{s0}^{-4} R\mathscr{R}^{7/2}),$$
$$\bar{p} \equiv p/(\rho_0 v_{s0}^2).$$

With these transformations, the MHD equations (2.1)–(2.4) remain unaltered, except that all quantities are equipped with a bar and that the quantity μ_0 disappears. Attention should be paid for the two dimensionless diffusion coefficients $\bar{\eta}_0$ and $\bar{\kappa}_0$. As they are very sensitive to the initial sound speed v_{s0}, a slight deviation in the assumed known initial value v_{s0} might lead to great changes in $\bar{\eta}_0$ and $\bar{\kappa}_0$. For the sake of brevity, we suppress the bars in the numerical study in Sec. 4.

3. The capillary discharge

3.1. Slow and fast capillary discharges

The gas-filled slow and the fast capillary discharges will be investigated separately in our numerical study. For the slow capillary discharge, an alumina (Al_2O_3) tube with a radius of $R_S = 150$ μm and a length of a few centimeters is prefilled with 50 torr hydrogen gas. The slow discharge can be initiated by a current pulse $I_S(t) = I_S^p \sin(\pi t/t_S)$, with a peak current $I_S^p = 300$ A and a half duration $t_S = 200$ ns.

For the fast capillary discharge, the capillary tube with a radius $R_F = 500$ μm and a length of a few centimeters is also made of alumina. This tube is prefilled with 1 torr helium gas initially. The discharge is triggered by a fast rising current I_F, with a peak current $I_F^p = 5$ kA and a risetime of $t_F/2 = 15$ ns. Our numerical model investigates the resulting variation of the radial density distribution in each tube, exploiting one-dimensional approximations that are appropriate for the large aspect ratio (length/radius).

There are three distinctive features in the two discharge channels: (1) the discharge mechanisms in the two capillary discharges are different; (2) the radius of the fast discharge tube ($R_F = 500$ μm) is much larger than that of the slow discharge one ($R_S = 150$ μm); and (3) one tube is prefilled with helium gas, and the other is prefilled with hydrogen gas. These differences in channel radius and composition are such that, as will be shown in our simulations, at guiding channel formation similar pressure levels and radial sizes for the guiding channels are reached. A segmented approach is then conceivable.

In the slow discharge stage, a low induced toroidal field (plasma $\beta = 2\mu_0 p/B_\theta^2 > 40$ at our starting point $t_i = 50$ ns) will invariably demand a nearly constant pressure distribution for force balance at each time step. Together with cooling at the wall, this leads to a concave plasma density in the capillary. In the fast discharge stage, a high current quickly ionizes the low-pressure helium gas. The classical pinch effect will result, since the strong toroidal magnetic field ($B_\theta = \mu_0 I_F^p/(2\pi R_F) \approx 2$ T) compresses the plasma radially inward resulting in a central guiding channel.

Owing to the fast imploding phase, it is not necessary to make the fast discharge tube as thin as the slow discharge one. The slow discharge capillary is prefilled with the hydrogen gas. As compared with the noble helium gas, hydrogen is easier to ionize. Hence the above-mentioned current is enough to fully ionize the hydrogen gas. However, the hydrogen is prone to desorption of pre-attached H_2 on the wall if the initial pressure is lower than 10 torr. The fast discharge capillary is prefilled with

https://doi.org/10.1017/S0022377805004241 Published online by Cambridge University Press

helium gas, a relatively high discharge current is needed to ionize the noble gas. The desorption of the helium gas is weak; besides, a fast imploding phase isolates the plasma from the wall. The initial pressure for the fast discharge can therefore be lowered to 1 torr.

3.2. Time scales and plasma dynamics

Our study on the dynamics of the slow discharge hydrogen plasma starts from a homogeneous plasma with the number density $n = 2.5 \times 10^{18}$ cm^{-3} and the temperature $T = 2$ eV, where 80% of the hydrogen is ionized, so that the mean molecular weight $\tilde{\mu} = 0.556$. For this initial condition, the relevant time scales are: the sound transit time $\tau_{\rm sound} = R_{\rm S}/v_{\rm sound} \approx 6$ ns (the sound speed $v_{\rm sound} = \sqrt{\gamma p/\rho}$), the Alfvén transit time $\tau_{\rm A} = R_{\rm S}/v_{\rm A} \approx 38$ ns (the Alfvén speed $v_{\rm A} = B/\sqrt{\mu_0 \rho}$), the resistive diffusion time $\tau_{\rm res} = \mu_0 R_{\rm S}^2/\eta \approx 0.42$ ns and the thermal energy diffusion time $\tau_{\rm thermal} = \rho \mathscr{R} R_{\rm S}^2/[(\gamma - 1)\kappa] \approx 463$ ns. In a weakly magnetized plasma, κ and η are isotropic, $\eta = 65 Z \ln\Lambda T^{-3/2}$ (Ω m), $\kappa = 2.4 \times 10^{-10}$ $(Z \ln\Lambda)^{-1} T^{5/2}$ (W m^{-1} K^{-1}), $[T] =$ K. The Coulomb logarithm $\ln\Lambda = 14.9 - 0.5 \ln(10^{-20} n_{\rm e}) + \ln T_{\rm e}$, $[n_{\rm e}] =$ m^{-3}, $[T_{\rm e}] =$ keV [20], which only weakly depends on the electron temperature and density. In our calculation, $\ln\Lambda = 3.6$.

Clearly, resistivity plays an important role since it is responsible for Ohmic heating of the plasma. Since resistivity and thermal conduction are temperature dependent, $\eta = \eta_0 T^{-3/2}$, $\kappa = \kappa_0 T^{5/2}$, increasing the temperature will slow down Ohmic heating but speed up thermal conduction. This will continue up to the point where they balance each other and the temperature reaches its maximum value. Since resistivity dominates, a globally varying current density profile is expected.

The dynamics of the fast helium discharge starts from a homogeneous plasma with electron number density $n_{\rm e} = 4.3 \times 10^{16}$ cm^{-3} and temperature $T = 20$ eV. Helium is assumed to have a degree of ionization of 1.3, which is equivalent to 70% singly and 30% doubly ionized helium, so that $\tilde{\mu} = 1.74$. The plasma in this stage is strongly magnetized ($\Omega_{\rm e}\tau_{\rm e} \sim 25$, where the electrons cyclotron frequency $\Omega_{\rm e} \equiv eB/m_{\rm e}$, and the collisional relaxation time of electrons $\tau_{\rm e} \approx 1.09 \times 10^{16}\, T_{\rm e}^{3/2}/(\ln\Lambda\, Z n_{\rm e})$, $[T_{\rm e}] =$ keV, $[n_{\rm e}] =$ m^{-3} [19]. Such a magnetic field has a strong effect on the transport properties in the transverse direction. The transverse radial thermal energy diffusion is inhibited, since the ratio of the thermal conductivities in the cross-field and field-aligned directions is $\kappa_\perp/\kappa_\parallel \sim (\Omega_{\rm e}\tau_{\rm e})^{-2} \ll 1$ [21]. The Alfvén transit time for the fast stage becomes $\tau_{\rm A} \approx 3.8$ ns, while the resistive diffusion time $\tau_{\rm res} \approx 35$ ns (the Coulomb logarithm $\ln\Lambda = 8$ in the expression for $\eta(T)$). Unlike the slow discharge stage, where resistive diffusion quickly leads to a diffuse current profile, in the fast discharge stage a current sheet is easily formed due to the long resistive diffusion time. Once a strong current sheet is formed, there is almost no thermal energy diffusion across the sheet. This leads to further heating of the plasma in the sheet and to a decrease of the resistivity, so that the plasma becomes unstable to a dynamic z-pinch effect on the ideal MHD time scale. Note that all of these time scales are evaluated at the starting points (corresponding to 50 ns for the slow discharge stage and 4.5 ns for the fast discharge stage).

4. Numerical study

The numerical code VAC (Versatile Advection Code) [22] has been used for our investigations. The code simulates plasma dynamics in the MHD approximation.

https://doi.org/10.1017/S0022377805004241 Published online by Cambridge University Press

It uses a finite-volume discretization of the system of MHD equations and a conservative shock-capturing scheme, namely the TVD scheme [23]. The non-ideal terms, which contain the diffusive coefficients κ and η, are treated as source terms.

4.1. Evolution of the slow discharge channel

4.1.1. Initial conditions and slow discharge current modeling. The simulation is performed in the radial variable (r) of a cylindrical coordinate system with axial symmetry ($\partial/\partial\theta = 0$), and it starts with a uniform density. The initial pressure is taken such that force balance holds in the radial direction:

$$\partial p/\partial r + j_z B_\theta = 0. \tag{4.1}$$

In the discharge circuit, the axial discharge current flowing along the capillary axis is externally controlled and depends on the capillary length, the external capacitor voltage, and the external circuit parameters (i.e. the external inductivity L and the external capacity C). The experiment enforces a current pulse $I_S(t) = I_S^p \sin(t\pi/t_S)$, which may have a certain radial distribution. The current density profile is rather flat close to the electrodes; we may assume $j_z(r,t) = j_{01}\sin(t\pi/t_S)$. In the central part of the capillary (away from the electrodes), the current will tend to flow in the high-temperature (low-resistivity) central region. Consequently, a high rate of Ohmic heating in this region will maintain a peaked current density [24]; we may assume $j_z(r,t) = j_{02}(1-\delta r^2)\sin(t\pi/t_S)$. Since our calculation is one-dimensional, we will present results for both assumptions on the current distributions. Because of the externally applied discharge current, instead of solving the induction equation (2.3), we impose a time-dependent magnetic field $B_\theta(r,t)$ in our simulations. The dimensionless parameters of the diffusion coefficients are $\eta_0 = 6.8$ and $\kappa_0 = 0.076$.

The initial conditions for the density ρ, the radial velocity v_r, the magnetic field B_θ and the thermal pressure p are:

$$\rho(r, t=0) = 1, \tag{4.2}$$

$$v_r(r, t=0) = 0, \tag{4.3}$$

$$B_\theta(r, t=0) = \frac{1}{2} j_0 r \left(1 - \frac{1}{2}\delta r^2\right) \sin\left(\frac{t_i}{t_S}\pi\right), \tag{4.4}$$

$$p(r, t=0) = \frac{1}{\gamma} - \frac{1}{4} j_0^2 r^2 \left(1 - \frac{3}{4}\delta r^2 + \frac{1}{6}\delta^2 r^4\right) \sin^2\left(\frac{t_i}{t_S}\pi\right). \tag{4.5}$$

4.1.2. Boundary conditions. Our calculation is performed on a one-dimensional uniform grid with $N = 150$ on $0 < r < 1$. At the symmetry axis $r = 0$, all fluxes vanish, and we use asymmetric boundary conditions for the radial and azimuthal vector components, while all the other variables are symmetric. At the wall ($r = 1$), the vector components orthogonal to the wall are zero (perfectly conducting wall), whereas the other variables are assumed to be symmetric, except for the temperature. The temperature at the wall is fixed to the low dimensionless value $T(r = 1) = 0.55$ (corresponding to about 1.8 eV).

4.1.3. Slow discharge dynamics. In general, a flat current density in the cold anode regime (Fig. 1) becomes steep in the central part of the channel due to the non-uniform temperature. Figure 1 quantifies the evolution of density and temperature

https://doi.org/10.1017/S0022377805004241 Published online by Cambridge University Press

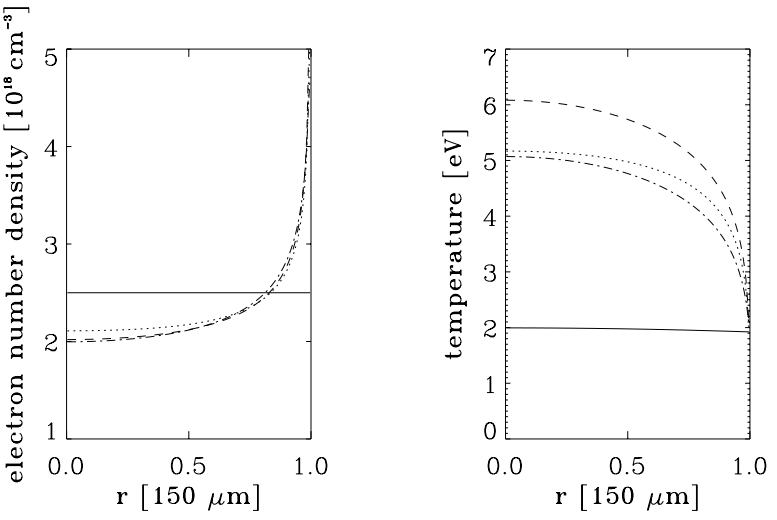


Figure 1. Electron density distribution and plasma temperature distribution for a slow discharge with flat current density $j_z(r,t) = j_{01}\sin(t\pi/t_S)$ at $t = 50$ ns (solid), $t = 60$ ns (dotted), $t = 100$ ns (dashed) and $t = 150$ ns (dash dot).

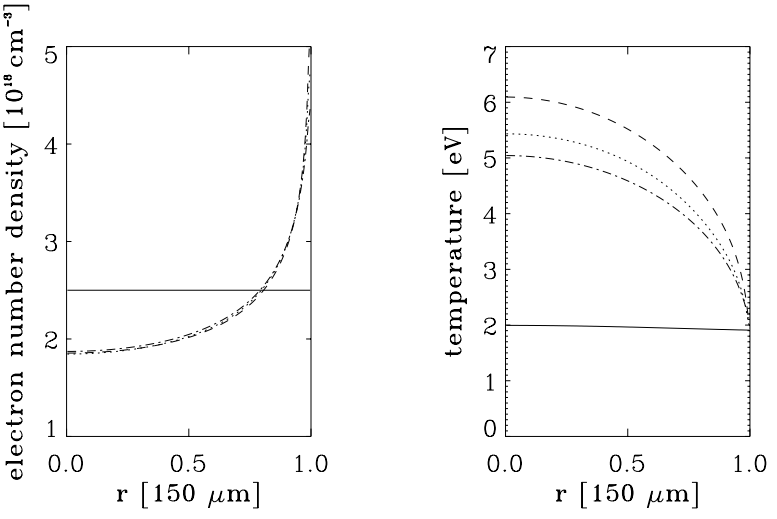


Figure 2. Electron density distribution and plasma temperature distribution with current density $j_z(r,t) = j_{02}(1-\delta r^2)\sin(t\pi/t_S)$ at $t = 50$ ns (solid), $t = 60$ ns (dotted), $t = 100$ ns (dashed) and $t = 150$ ns (dash dot).

profiles beyond $t_i = 50$ ns under the assumption of a flat current density profile $j_z(r,t) = j_{01}\sin(t\pi/t_S)$ with $j_{01} = j_0 = 0.44$, $\delta = 0$. In the central part of the channel (see Fig. 2), the current density is given by $j_z(r,t) = j_{02}(1-\delta r^2)\sin(t\pi/t_S)$ with $j_{02} = j_0 = 0.586$, $\delta = 0.5$. A deeper parabolic plasma channel (with $n_e(r = 0) = 1.8 \times 10^{18}$ cm^{-3}) is achieved soon after 60 ns, and it remains steady up to the end of our simulation time at 150 ns. Close to the cold anode region, a steady parabolic channel comes later (Fig. 1), and the density is about 10% higher than in the central part of the channel. The two different current density distributions

https://doi.org/10.1017/S0022377805004241 Published online by Cambridge University Press

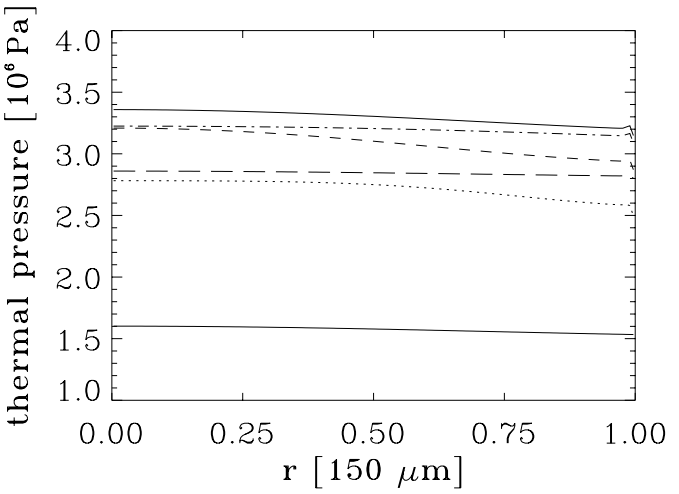


Figure 3. Thermal pressure distribution at $t = 50$ ns (solid), $t = 60$ ns (dotted), $t = 70$ ns (dashed), $t = 80$ ns (dash dot), $t = 100$ ns (dash dot dot) and $t = 150$ ns (long dash) for the slow discharge evolution from Fig. 2.

result in quite similar parabolic density profiles. The formation of a guiding channel depends weakly on $j_z(r)$.

In what follows, we will focus on the central part of the channel which starts its evolution with the more pronounced axial current profile $j_z(r,t) = j_{02}(1 - \delta r^2)\sin(t\pi/t_S)$. In Fig. 3, the thermal pressure of the plasma is plotted versus the radius at different times. The thermal pressure rises quickly as a result of Ohmic heating. Before about 70 ns, the thermal pressure is higher near the axis than at the wall since the edge region is thermally cooled. However, the radial force balance rather quickly (at 80 ns) forces the pressure to level off to a near constant value over the whole domain. The density profile is then inversely correlated to the temperature profile. Hence the channel is formed due to cooling of the plasma at the wall. A steady state is reached where

$$\eta j^2 + \frac{1}{r}\frac{\partial}{\partial r}\left(r\kappa\frac{\partial T}{\partial r}\right) = 0. \tag{4.6}$$

Figure 4 shows the radial velocity and the corresponding Mach number at different times. The plasma bounces on the acoustic time scale between the axis and the wall as a result of the changing pressure distribution before 80 ns, with the amplitude of each successive bounce becoming smaller. An almost steady plasma channel forms when this radial motion damps out and becomes dynamically insignificant beyond 70 ns. Note that, at all times, the radial motion remains subsonic so that no strong compression effects occur, as can be seen from the absence of strong oscillations in the plasma density distribution.

4.1.4. A segmented slow capillary discharge. Suppose that the slow discharge part is additionally separated into segments as suggested in [13]. A discharge current along, for example, four segments, can be increased sequentially. We study such a slow discharge setup numerically with the discharge currents of 300, 400, 500 and 600 A on the four segments, respectively. Our MHD simulations then reveal that a

https://doi.org/10.1017/S0022377805004241 Published online by Cambridge University Press

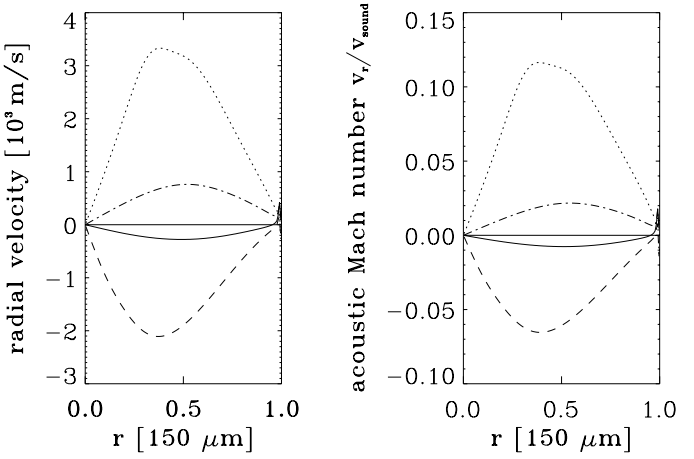


Figure 4. Radial velocity profiles (left) and corresponding acoustic Mach number (right) at 50 ns (solid), 55 ns (dotted), 58 ns (dashed), 70 ns (dash dot) and 80 ns (dash dot dot), for the simulation from Figs 2 and 3.

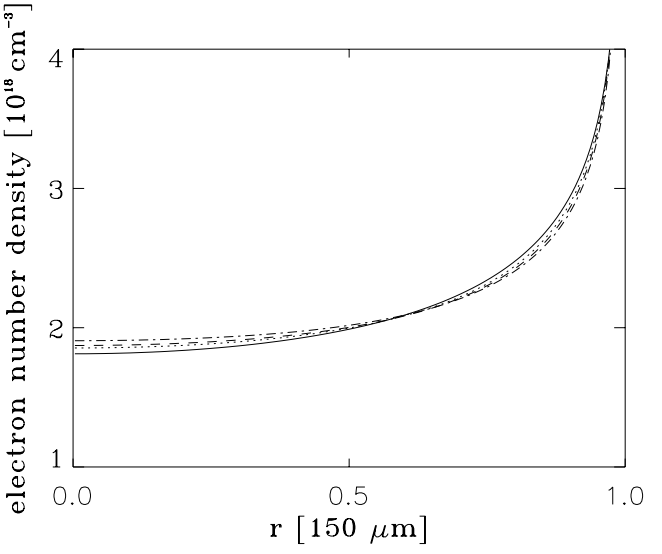


Figure 5. Electron density distributions for four different currents: 300 A (solid), 400 A (dotted), 500 A (dashed) and 600 A (dash dot) at 80 ns.

quasi-steady density profile with an on-axis minimum is formed in each segment. Figure 5 shows the density distributions for the different discharge currents. An increase in discharge current results in only a very weak increase in the plasma density on-axis. By increasing the discharge current from 300 to 600 A, one obtains a weak density variation along the axis of the segmented setup. To effectively mitigate the dephasing problem, a magnitude of one order increase in the density within a few centimeters along the axis is required [12]. For this sequential slow discharge, the resulting weak density variation along the axis would fail to eliminate the dephasing problem in an LWFA.

https://doi.org/10.1017/S0022377805004241 Published online by Cambridge University Press

4.2. Fast discharge dynamics

The initial stage of a fast discharge stage has been studied numerically by Hosokai et al. [2] using the numerical code MULTI [25]. In the fast discharge stage, the capillary can be an alumina tube with an inner radius of 500 μm and length of a few centimeters. The tube is initially filled with helium gas at 1 torr. The discharge is driven by a quickly rising current with a peak of 5 kA and a risetime of 15 ns. In the first few nanoseconds (∼5 ns), the discharge current starts flowing near the wall. The plasma temperature rises up to 20 eV and the helium gas is strongly (about 70% singly and 30% doubly) ionized.

In our MHD model, we study the plasma dynamics after 4.5 ns when significant ionization is reached [2]. At the prevailing conditions, the electron density $n_e \approx 4.3 \times 10^{16}$ cm^{-3}. The conductivity of the almost fully ionized helium near the wall is higher than the conductivity of the still partially ionized helium near the axis. The discharge current is peaked near the wall. Because of slow diffusion ($\tau_{res} < \tau_A$), a current sheet develops.

In our numerical study of the fast discharge stage, the initial conditions for all the physical quantities are:

$$\rho(r, t = 0) = 1, \tag{4.7}$$

$$v_r(r, t = 0) = 0, \tag{4.8}$$

$$B_\theta(r, t = 0) = \tfrac{1}{2} j_0^F r(1 + 2r^4), \tag{4.9}$$

$$p(r, t = 0) = \frac{1}{\gamma}. \tag{4.10}$$

Unlike the slow discharge stage, where we impose a time-dependent $B_\theta(r, t)$, here we initially give a value to the magnetic field $B_\theta(r, t = 0)$ and solve all the MHD equations including the induction equation (2.3). We use a uniform grid with $N = 900$ on $0 < r < 1$, and the parameter $j_0^F = 1.86$ for the fast discharge simulation.

In this strongly magnetized plasma, the transverse thermal conduction $\kappa_\perp$ is negligible, so that cooling by the wall is effectively prohibited. Hence, the temperature at the wall is no longer fixed and we prescribe a zero gradient condition $T' = 0$. All the other variables have the same boundary conditions as in the slow capillary discharge. We still use the classical Spitzer resistivity; the dimensionless diffusion parameter $\eta_0 = 0.14$.

Figure 6 shows the electron density distribution before (upper part) and after (lower part) the pinch time (∼9.2 ns), defined as the time when the radial implosion reaches the axis. Before that time, the plasma is compressed inwardly by the strong azimuthal magnetic field. For times less than 7.8 ns, the density is low and the density peak is far from the axis. This is not optimal for guiding a laser beam. When the plasma column compresses to ∼150 μm in radius at 7.8 ns, a suitable guiding channel starts to form of similar radial extent as the slow discharge stage, while the plasma density at this moment is still rather low: $n_e \sim 0.5 \times 10^{17}$ cm^{-3} on-axis. As the plasma column continues its compression, both the density and the density contrast between the peak and the axial value of the plasma channel increase, and efficient beam guiding is expected between 7.8 and 9.0 ns. Then the plasma column collapses on the axis at around 9.2 ns, at which point the temperature reaches its maximum value, exceeding 80 eV (see Fig. 7). From that point on, the desired guiding is lost due to the convexity of the plasma density profile. Shortly after the

https://doi.org/10.1017/S0022377805004241 Published online by Cambridge University Press

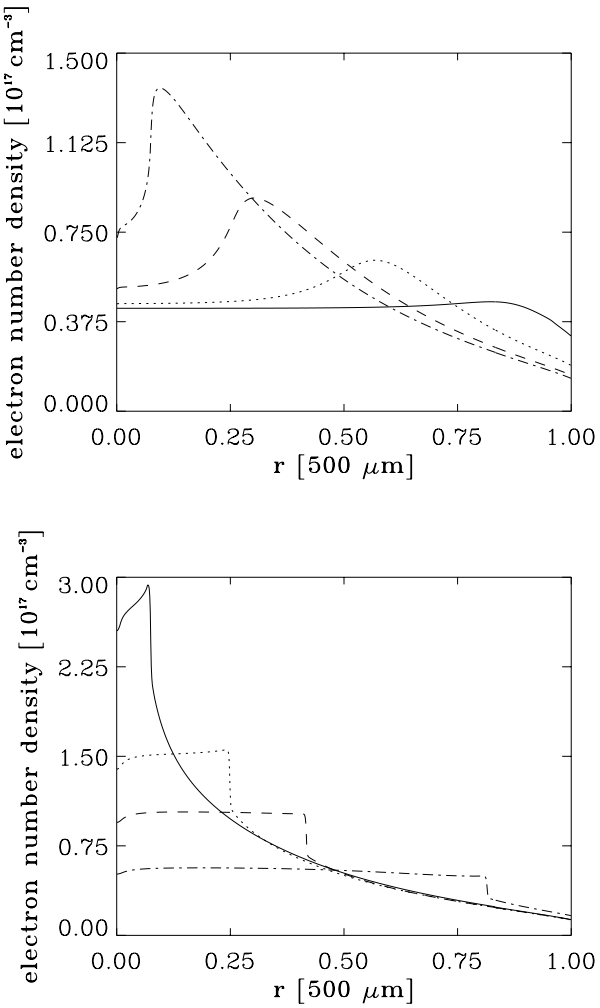


Figure 6. Upper: electron density distribution at 5.0 ns (solid), 6.4 ns (dotted), 7.8 ns (dashed) and 8.7 ns (dash dot). Lower: electron density distribution at 9.4 ns (solid), 10.4 ns (dotted), 11.3 ns (dashed) and 13.6 ns (dash dot).

collapse on the axis, the rebound causes the inner part of the plasma to expand, while the outer part of the plasma still moves radially inwards (see the dashed line at 9.4 ns in Fig. 8). After the axial rebound, a strong shock wave moves outward (the Mach number $M = v_{\rm shock}/v_{\rm sound} = 1.4$). A weak second guiding might be obtained during the first stage of the rebound phase when an off-axis density peak moves outward. The second guiding phase is rather short and lasts for about 1.5 ns only.

The dynamics of the fast discharge can be described by the imbalance between the thermal pressure and the magnetic pressure. It is a pure z-pinch effect. The Lorentz force accelerates the plasma inward onto the axis. As the plasma is compressed, the plasma becomes hotter due to the Ohmic heating and shock heating and the thermal pressure increases. When the thermal pressure balances the magnetic pressure, the plasma stagnates and then expands.

https://doi.org/10.1017/S0022377805004241 Published online by Cambridge University Press

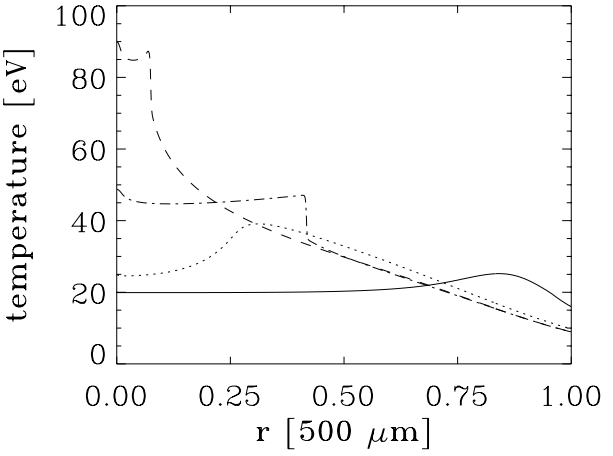


Figure 7. Temperature profile at 5.0 ns (solid), 7.8 ns (dotted), 9.4 ns (dashed) and 11.3 ns (dash dot).

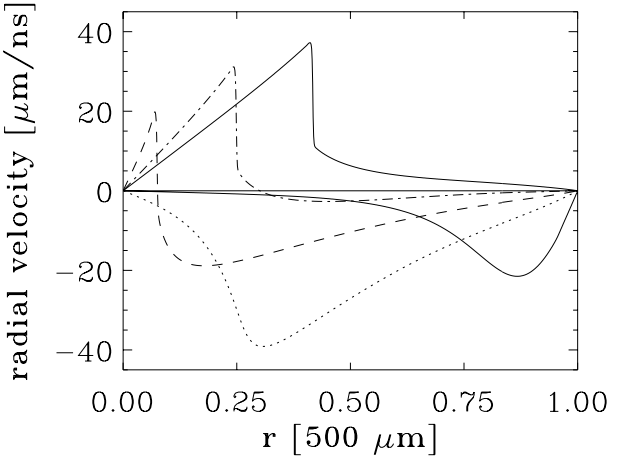


Figure 8. Radial velocity profiles at 5.0 ns (solid), 7.8 ns (dotted), 9.4 ns (dashed), 10.4 ns (dash dot) and 11.3 ns (dash dot dot).

5. Conclusions and discussions

We have investigated numerically the dynamics of both the slow discharge plasma channel and the fast discharge plasma channel. The modeling of these two plasma channels considers the MHD processes following their initial discharge and ionization processes. Our numerical studies shows that the slow discharge channel is essentially steady with a density minimum on-axis [$n_e(0) = 2 \times 10^{18}$ cm^{-3}]. Such a guiding channel can last for more than 100 ns—long enough for any laser pulse passing through it.

The fast discharge channel has a rather dynamic imploding process. A strong azimuthal field induced by a wall-concentrated discharge current compresses plasma inwards much like a snowplough effect. Such a z-pinch channel formation results in a very dynamic guiding channel. The channel suitable for guiding lasts only a

https://doi.org/10.1017/S0022377805004241 Published online by Cambridge University Press

few nanoseconds. So that timing the pulse through the channel becomes important here.

The fast capillary discharge provides us a guiding channel with a density $n_e \sim 5 \times 10^{16}$ cm^{-3}, around two orders of magnitude lower than the density in the slow discharge channel. The low density greatly lengthens the corresponding plasma wavelength, $\lambda_p \sim 0.15$ μm. Such a millimeter plasma wave lowers the femtosecond timing restriction on the beam injection.

Due to the different features of these two plasma channels, it is possible to get a tapered plasma density by joining these two tubes. As mentioned in the first section, the dephasing problem can be overcome by a tapered channel and experiments using a segmented approach have been presented [13]. At channel formation, both slow and fast discharge channels are at about 10^6 Pa, and the guiding channel is concave over 150 μm. The large density contrast could be beneficial for tapered axial density approaches, and our results show that combining slow discharge capillaries alone only marginally increases the on-axis densities. Because of the relatively slow phase velocity of the wakefield, the accelerated electrons out run the accelerating field. A plasma density increase along the channel provides a possibility to keep accelerated electrons in phase with the accelerating wakefield over many dephasing lengths. So that a joined two-stage capillary discharge where a fast capillary segment is followed by a slow one is an attractive proposal.

So far, we have been considering problems with cylindrical symmetry, i.e. problems in which all parameters depend only on r. Perfect cylindrical symmetry cannot be reproduced in real life, even if the system is magnetohydrodynamically stable [26]. Indeed, the pinch always has a finite length, and there is contact between the pinch plasma and the electrodes. This creates some axial non-uniformity, which requires multidimensional modeling. To better understand the plasma dynamics inside real capillaries, multidimensional effects will be investigated in the future.

In our numerical studies, the degree of ionization is a free parameter. For the slow capillary discharge, the ionization might reduce due to the relatively cold wall as shown by Broks et al. [17]. Since our study starts from the point when the gas is almost fully ionized, and since the partially ionized gas is limited to a narrow wall region, our simulations for the main part of the channel agree well with both experimental measurement and other simulations. For the fast discharge, the plasma compression is accompanied by an increase of the temperature and an increase of the ionization degree. Helium might be fully ionized shortly before the pinch time; the electron density n_e from our simulation might be 35% lower than the experimental result.

The next few paragraphs will be devoted to a discussion concerning the general applicability of the fluid model that is used for simulations in this paper. To justify the one fluid description:

- the electrons and ions must undergo frequent collisions. The time scale of the plasma evolution τ_H should be much longer than the collisional relaxation times for electrons τ_e and ions τ_i: $\tau_H \gg \tau_i$ ($\gg \tau_e$);
- the length scale a of the plasma dynamics should be much larger than the minimum size over which the condition of quasi charge-neutrality holds ($a \gg \lambda_D$), but also much larger than the ion cyclotron radius: $a \gg R_i$, whereas the time scale should be much longer than the inverse ion cyclotron frequency: $\tau_H \gg \Omega_i^{-1}$.

https://doi.org/10.1017/S0022377805004241 Published online by Cambridge University Press

The collisional time $\tau_i \approx 4.66 \times 10^{17} A^{1/2} T_i^{3/2}/(\ln \Lambda Z^3 n_e)$, $[T_i] = \mathrm{keV}$, $[n_e] = \mathrm{m}^{-3}$, where A is the mass number and Z is the charge number [19].

For the slow discharge capillary, the time scale of the plasma evolution $\tau_H \approx t_S/2 = 1.0 \times 10^{-7}$ s and the collisional time $\tau_i = 4.3 \times 10^{-12}$ s, so that the first condition is satisfied. For the fast discharge segment, the collisional time for ions $\tau_i = 1.0 \times 10^{-9}$ s and the time scale of the plasma evolution $\tau_H \approx t_F/2 = 1.5 \times 10^{-8}$ s, which is only one order of magnitude larger than the collisional time τ_i.

However, the conditions on the space and time scales with respect to the ion cyclotron radius and inverse frequency are not really satisfied, both in the slow and in the fast discharge states. Hence, whereas our fluid modeling gives a qualitatively correct picture of the dynamics, further kinetic modeling is in order.

Acknowledgements

The authors thank Bart Broks and Albert Reitsma for fruitful discussions. This work was performed as part of the research program of 'Stichting voor Fundamenteel Onderzoek der Materie' (FOM) with financial support from NWO, within the FOM program 55 on Laser Wakefield Accelerations.

References

[1] Taijma, T. and Dawson, J. 1979 *J. Phys. Rev. Lett.* **43**, 267.

[2] Hosokai, T., Kando, M., Dewa, H., Kotaki, H., Kondo, S., Hasegawa, N., Nakajima, K. and Horioka, K. 2000 *Opt. Lett.* **25**, 10.

[3] Spence, D. J. and Hooker, S. M. 2000 *Phys. Rev.* E **63**, 015 401.

[4] Luther, B. M., Wang, Y., Marconi, M. C., Chilla, J. L. A., Larotonda, M. A. and Rocca, J. J. 2004 *Phys. Rev. Lett.* **92**, 235 002.

[5] Tzeng, K. C., Mori, W. B. and Katsouleas, T. 1997 *Phys. Rev. Lett.* **79**, 5258.

[6] Gordon, D. et al. 1998 *Phys. Rev. Lett.* **80**, 2133.

[7] Esarey, E., Hafizi, B., Hubbard, R. and Ting, A. 1998 *Phys. Rev. Lett.* **80**, 5552.

[8] Mangles, S. P. D. et al. 2004 *Nature* **431**, 535.

[9] Geddes, C. G. R., Toth, Cs., van Tilborg, J., Esarey, E., Schroeder, C. B., Bruhwiler, D., Nieter, C., Cary, J. and Leemans, W. P. 2004 *Nature* **431**, 538.

[10] Faure, J., Glinec, Y., Pukhov, A., Kiselev, S., Gordienko, S., Lefebvre, E., Rousseau, J. P., Burgy, F. and Malka, V. 2004 *Nature* **431**, 541.

[11] Katsouleas, T. 1986 *Phys. Rev.* A **33**, 2056.

[12] Sprangle, P., Hafizi, B., Penano, J. R., Hubbard, R. F., Ting, A., Zigler, A. and Antonsen, T. M. 2000 *Phys. Rev. Lett.* **85**, 5110.

[13] Kaganovich, D., Zigler, A., Hubbard, R. F., Sprangle, P. and Ting, A. 2001 *Appl. Phys. Lett.* **78**, 3175.

[14] Ting, A., Esarey, E. and Sprangle, P. 1990 *Phys. Fluids* B **2**, 1390.

[15] Dorchies, F. et al. 1999 *Phys. Plasmas* **6**, 2903.

[16] Bobrova, N. A., Esaulov, A. A., Sakai, J. I., Sasorov, P. V., Spence, D. J., Butler, A., Hooker, S. M. and Bulanov, S. V. 2002 *Phys. Rev.* E **65**, 016 407.

[17] Broks, B. H. P., Garloff, K. and van der Mullen, J. J. A. M. 2005 *Phys. Rev.* E **71**, 016401.

[18] Spitzer, L. Jr. 1962 *Physics of Fully Ionized Gases*. New York: Wiley.

[19] Goedbloed, J. P. and Poedts, S. 2004 *Principles of Magnetohydrodynamics*. Cambridge: Cambridge University Press.

https://doi.org/10.1017/S0022377805004241 Published online by Cambridge University Press

[20] Wesson, J. 1987 *Tokamaks*. Oxford: Clarendon Press.
[21] Braginskii, S. I. 1965 *Rev. Plasma Phys.* **1**.
[22] Tóth, G. 1996 *Astrophys. Lett. Commun.* **34** 245, http://www.phys.uu.nl/∼toth.
[23] Harten, A. 1983 *J. Comput. Phys.* **49**, 357.
[24] Coppins, M. 1988 *Plasma Phys. Controlled Fusion* **30**, 201.
[25] Ramis, R., Schmalz, R. and Meyer-ter-Vehn, J. 1988 *Comput. Phys. Commun.* **49**, 475.
[26] Wang, C., Keppens, R. and Goedbloed, J. P. 2003 *J. Phys.* D **36**, 2255.

https://doi.org/10.1017/S0022377805004241 Published online by Cambridge University Press